Research in Astronomy and Astrophysics, 23:015002 (14pp), 2023 January https://doi.org/10.1088/1674-4527/ac9f07

Photometric Properties and Stellar Parameters of the Rapidly Rotating Magnetic Early-B Star HD 345439

Dong-Xiang Shen[1], Jin-Zhong Liu[2], Chun-Hua Zhu[1], Guo-Liang Lü[1], Yu Zhang[2], Cheng-Long Lü[2], Hao-Zhi Wang[2], Lei Li[1], Xi-Zhen Lu[1], Jin-Long Yu[1], and Abdurepqet Rustem[1]
[1] School of Physical Science and Technology, Xinjiang University, Urumqi 830046, China; chunhuazhu@sina.cn
[2] Xinjiang Astronomical Observatory, National Astronomical Observatories, Chinese Academy of Sciences, Urumqi 830000, China; liujinzh@xao.ac.cn
Received 2022 August 22; revised 2022 October 11; accepted 2022 October 24; published 2022 December 9

Abstract

We first present the multicolor photometry results of the rapidly rotating magnetic star HD 345439 using the Nanshan One-meter Wide-field Telescope. From the photometric observations, we derive a rotational period of 0.7699 ± 0.0014 day. The light curves of HD 345439 are dominated by the double asymmetric S-wave feature that arises from the magnetic clouds. Pulsating behaviors are not observed in Sector 41 of the Transiting Exoplanet Survey Satellite. No evidence is found of the occurrence of centrifugal breakout events neither in the residual flux nor in the systematic variations at the extremum of the light curve. Based on the hypothesis of the Rigidly Rotating Magnetosphere model, we restrict the magnetic obliquity angle β and the rotational inclination angle i so that they satisfy the approximate relation $\beta + i \approx 105°$. The color excess, extinction, and luminosity are determined to be $E_{(B-V)} = 0.745 \pm 0.016$ mag, $A_V = 2.31 \pm 0.05$ mag, and $\log(L/L_\odot) = 3.82 \pm 0.1$ dex, respectively. Furthermore, we derive the effective temperature as $T_{\rm eff} = 22 \pm 1$ kK and the surface gravity as $\log\ g = 4.00 \pm 0.22$. The mass $M = 7.24^{+1.75}_{-1.24}\ M_\odot$, radius $R = 4.44^{+2.68}_{-1.93}\ R_\odot$, and age $\tau_{\rm age} = 23.62^{+4.24}_{-21.97}$ Myr are estimated from the Hertzsprung–Russell diagram.

Key words: stars: chemically peculiar – stars: early-type – stars: fundamental parameters – stars: magnetic field

1. Introduction

Since pioneering detections of the strong magnetic fields in the chemically peculiar Ap/Bp stars (Babcock 1947; Borra & Landstreet 1980), new generations of spectropolarimeters have detected large-scale, systematic magnetic fields in numerous massive stars (e.g., Bagnulo et al. 2003; Petit et al. 2004; Bailey et al. 2011; Wade et al. 2012b, 2012a; Fossati et al. 2015; González et al. 2019). In recent years, the Magnetism in Massive Stars (MiMeS; Wade et al. 2009) and B fields in OB stars (BOB; Hubrig et al. 2014) projects have detected dozens of new magnetic OB stars successively; a proportion of these magnetic stars have also been revealed using high-resolution spectroscopy (e.g., Wade et al. 2006; Wade et al. 2012a, 2015). The observations indicate that magnetic stars exhibit unique phenomena, such as cyclic variability in line profile morphologies (e.g., Folsom et al. 2010; Hubrig et al. 2017b; Shultz & Wade 2017), X-ray emission (e.g., Schnerr et al. 2008; Oskinova et al. 2011), and light curve variations (e.g., Fossati et al. 2014; González et al. 2019; Shultz et al. 2021). The behaviors that magnetic fields cause in massive stars, for instance, magnetic field evolution, mass-loss quenching, and magnetic braking, are of utmost importance to understanding the evolution of magnetic stars.

Being a typical helium-rich massive star, HD 345439 shows extremely strong, large-scale magnetic fields and fast rotation (Eikenberry et al. 2014). The longitudinal magnetic fields of HD 345439 have a periodic variability with an amplitude of 2–3 kG, and the polar magnetic strength reaches 10 kG (Hubrig et al. 2017a). To date, only several analogs have been discovered: HR 7355 (Rivinius et al. 2008), HR 5907 (Grunhut et al. 2012), HD 23478 (Wisniewski et al. 2015), σ Ori E (Landstreet & Borra 1978), HD 176582 (Bohlender & Monin 2011), δ Ori C (Leone et al. 2010), HD 35502 (Sikora et al. 2016), and HD 164492C (Wade et al. 2017; González et al. 2017). The observations indicate that strong magnetic fields may contribute to material accumulation and the formation of a high-density disk (Carciofi et al. 2013; Oksala et al. 2015). On the other hand, the magnetic field seems to result in an enhanced He absorption and an inhomogeneous spatial distribution of the elements in the photosphere (e.g., Grunhut et al. 2012; Rivinius et al. 2013). Other physical manifestations of the magnetosphere were detected in observations of X-ray, ultraviolet(UV), and radio observations (e.g., Leto et al. 2018).

Recently, the Rigidly Rotating Magnetosphere (RRM) model has been developed to explain the variability of magnetic stars (Townsend et al. 2005; Townsend & Owocki 2005). The RRM model provides an empirical picture according to which plasma is predominantly subjected to gravity and the centrifugal force. Furthermore, the plasma originated from stars is constrained to move along the magnetic field lines. The gravitational force

prompts the material to infall toward the star, while the centrifugal force acts in the opposite manner. Based on the assumptions of the RRM model, there is a point for each magnetic field line where the gravitational plus centrifugal potential reaches the minimum value required for causing the material accumulation. The disk consisting of the accumulated material produces the eclipse morphology in the light curves of σ Ori E type stars (Oksala et al. 2015). Until now, only σ Ori E has been characterized using photometry, spectropolarimetry, and spectrometry. Here, we aim to provide more detailed characteristics of the rapidly rotating magnetic early-type star HD 345439 using NOWT photometric observations.

We introduce the observations of the photometric and spectrometric data in Section 2 of this article. In Section 3, we determine the rotational period, pulsating behavior, variations in the light curves, centrifugal breakout, and stellar parameters of HD 345439 from the collected data sets and the theoretical model. In Section 4, we discuss the results derived from the observations. Finally, the conclusions are provided in Section 5.

2. Observations and Data Reduction

2.1. Multicolor Photometric Observations

The multicolor photometric measurements of HD 345439 were performed using the Nanshan One-meter Wide-field Telescope (NOWT; Bai et al. 2020; Shen et al. 2021) of the Xinjiang Astronomical Observatory (XAO), Chinese Academy of Sciences (CAS). NOWT is an alt-azimuth mount reflector telescope at Nanshan in Xinjiang. NOWT is equipped with a 4096×4136-pixel CCD and a Johnson–Cousins *UBVRI* filter system. The CCD provides a field of view (FoV) of 1.3×1.3 degree^2, and the per-pixel resolution is $1\farcs28$. The photometric observations were performed over a period of 12 nights from 2020 October 13 to November 12, and 2457 frames of HD 345439 were obtained. During the observations, when a single exposure of one band was finished, the filter wheel rotated to the next band. The FoV of the CCD readout was set as 42.67×42.67 arcmin^2 to ensure the efficiency of the observations, and the scan rate mode was set to medium. The observations were supplemented with a series of 10 bias and three flat-field exposures per filter every night to calibrate the CCD instrumental signature. The observing log is summarized in Table 1.

The data reductions, including bias subtraction, flat-fielding, and illumination correction, were carried out using the CCDPROC task of the Image Reduction and Analysis Facility (IRAF[3]) software. Part of one observation image is shown in Figure 1, where HD 345439, the comparison star, and the check star are indicated. Differential photometry was carried out by using the standard aperture photometric package of the IRAF APPHOT task. The photometric error distribution is shown in Figure 2. Although the photometric error in the *U* band is considerably higher than that in the other bands, the overall multicolor photometry process is stable.

2.2. Archival Data

The archival photometric data of HD 345439 employed in this work were obtained from the All-Sky Automated Survey for Supernovae (ASAS-SN; Kochanek et al. 2017; Jayasinghe et al. 2018; Pawlak et al. 2019), the Super Wide Angle Search for Planets (SuperWASP; Butters et al. 2010), and the Transiting Exoplanet Survey Satellite (TESS; Ricker et al. 2015). The ASAS-SN was the first project to routinely survey the entire visible sky in the *V* band, reaching a depth of roughly 17 mag. As of the mid-2017, ASAS-SN consists of two observing stations, namely the Haleakala Observatory (Hawaii) and the Cerro Tololo International Observatory (CTIO, Chile) sites. By the end of 2017, ASAS-SN expanded to comprise five observing stations with the addition of a second unit at the CTIO and two more units at the McDonald Observatory (Texas) and the South African Astrophysical Observatory (SAAO, Sutherland, South Africa). Two observational data sets were obtained from the ASAS-SN Photometry Database[4] using different sources. In the first observational data set, ASAS-SN observed HD 345439 using the APOGEE input catalog; 349 photometric data points were obtained from 2015 February to 2018 April using bc and bd cameras. In the second observational data set, the observations were conducted using the ASAS-SN DR9 source and the bc camera and consisted of 192 epochs from February 2015 to October 2018. SuperWASP is an extra-solar planet detection program employing identical robotic telescopes. The telescopes are equipped with a 2048×2048 thinned CCD with a pixel size of 13.5 μm. SuperWASP carried out observations of HD 345439 over 67 nights in 2007 and provided 979 points of photometric observations in a broadband filter (bandpass from 400 to 700 nm). TESS is a NASA Astrophysics Explorer mission. The satellite is equipped with four identical wide-field cameras, which together can monitor the sky. TESS conducted photometric observations of HD 345439 in Sector 41 with a 2 minutes cadence mode, providing the most complete light curve of the star. The photometric data of TESS was reduced using the lightkurve package (hereafter denoted as LK).[5]

The Large Sky Area Multi-Object Fiber Spectroscopic Telescope (LAMOST; Cui et al. 2012) is a refecting Schmidt telescope located at the Xinglong station of the National Astronomical Observatories, Chinese Academy of Sciences. The mean aperture of the LAMOST is 4.3 m, and

[3] IRAF is distributed by the National Optical Astronomy Observatories, which are operated by the Association of Universities for Research in Astronomy, Inc., under cooperative agreement with the National Science Foundation.

[4] https://asas-sn.osu.edu/variables

[5] http://docs.lightkurve.org/

Table 1
Summary of Photometric Observations with NOWT

Date	*U* Exp. 45 s	*B* Exp. 10 s	*V* Exp. 7 s	*R* Exp. 7 s	*I* Exp. 8s	Weather
2020 Oct 13	60	59	58	57	57	P.
2020 Oct 14	59	58	59	59	57	P.
2020 Oct 15	40	36	36	35	35	P.
2020 Oct 16	63	67	63	62	62	P.
2020 Oct 17	55	56	63	52	52	P.
2020 Oct 18	35	36	36	36	36	P.
2020 Oct 19	55	55	55	55	55	P.
2020 Oct 20	47	47	46	46	45	P.
2020 Oct 21	43	41	42	41	41	P.
2020 Nov 8	6	6	6	5	6	C.
2020 Nov 11	19	19	19	19	19	C.
2020 Nov 12	17	15	16	16	16	C.

Note. This table summarizes the situations of photometric observations of NOWT. The number of frames for different filters in each night are listed, respectively. The exposure times are listed under the filter name. In the last column, we marked the weather of each observing night, P. represents the relatively good night, and the Full Width at Half Maximum (FWHM) of HD 345439 less than 2.8, and C. represents the cloudy night, with the FWHM of HD 345439 less than 3.5 and larger than 2.8.

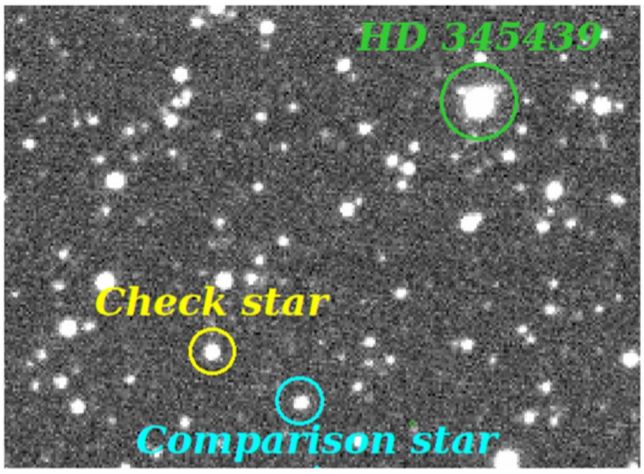

Figure 1. Part of one observation image, where HD 345439, the comparison star, and the check star are indicated.

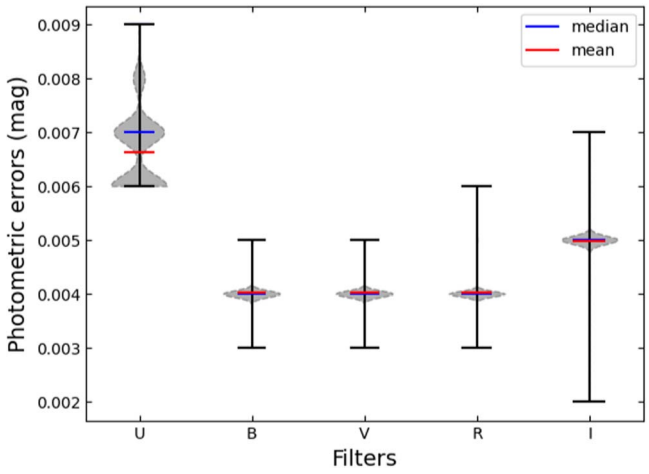

Figure 2. Photometric error distribution of each multicolor photometry filter. The error bars represent the maximum and minimum values of the photometric errors. The gray areas represent the kernel density distribution of the photometric errors. The red and blue segments represent the mean and median values of the photometric errors, respectively.

the corresponding FoV is 5° in diameter (Luo et al. 2015). A low-resolution spectrum of HD 345439 was obtained in the LAMSOT Low-Resolution Survey Data Release 7 (LAMOST-LRS DR7).[6]

3. Results

3.1. Rotational Period

To fit the He I line profiles, Eikenberry et al. (2014) hypothesized that the rotational velocity $v\sin i$ has a value of $270 \pm 20\,\mathrm{km\,s^{-1}}$. Wisniewski et al. (2015) derived a rotational period of 0.7701 day from the KELT, SuperWASP, and ASAS surveys. In this work, we determine the rotational period of HD 345439 by analyzing the new archival data and new photometric observations. The Lomb-Scargle method (Lomb 1976; Scargle 1982) provided by Astropy (Astropy Collaboration et al. 2013, 2018) was used to detect the periodic signals in the unevenly spaced SuperWASP and ASAS-SN observations. The PERIOD04 software (Lenz & Breger 2005) was used to detect the periodic signature in both the TESS and NOWT photometric observations. The validity of the frequencies that detected in the TESS and NOWT photometric observations has followed the example of Breger et al. (1993). The period-power spectra and corresponding light curves of the archival data are shown in Figure 3.

[6] http://dr7.lamost.org/

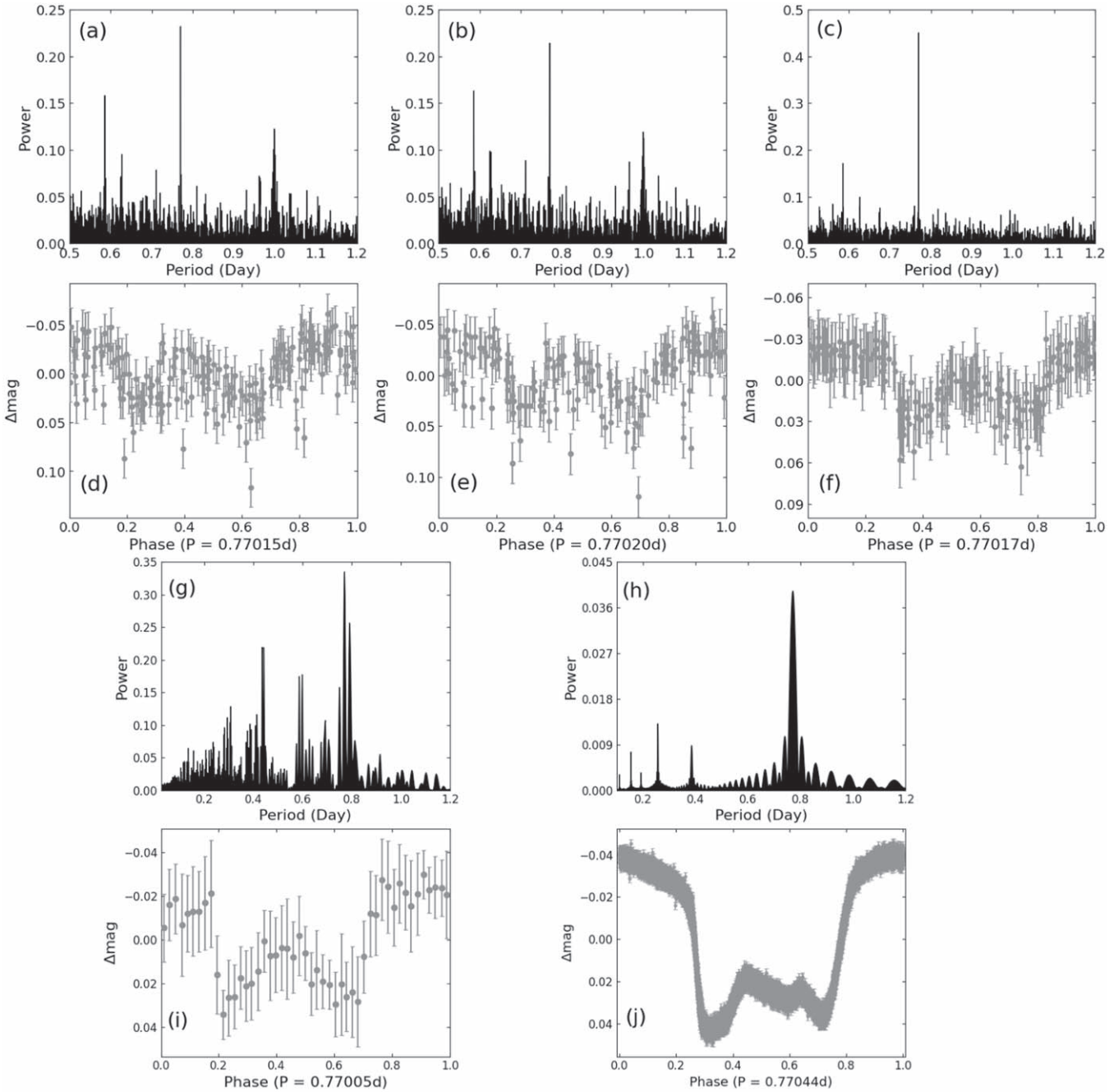

Figure 3. Periodograms (upper panels) and corresponding phase diagrams (bottom panels) of each archival data set of HD 345439. Panel (a) shows the periodic spectrum of the observations of ASAS-SN with the source of ASAS-SN DR9. Panel (b) shows the periodic spectrum of the ASAS-SN observations (with the APOGEE source) using the bc camera, while panel (c) illustrates the periodic spectrum of the ASAS-SN observations (with the APOGEE source) using the bd camera. The homologous phase diagrams are listed at the bottom of each periodic spectrum. The same diagrams for SuperWASP and TESS data are shown in panels (g) to (j).

The LombScargle periodogram of ASAS-SN using the ASAS-SN DR9 source shows that the rotational period exhibits a distinct signature at 0.7701 ± 0.0002 day. The value of 0.7702 ± 0.0001 day was derived from the ASAS-SN observations using the APOGEE source with the bc camera. A consistent periodic signal with a value of $0.770\,17 \pm 0.00013$ day appears also in the ASAS-SN measurements using the bd camera. The SuperWASP photometric data also reveal a rotational period of 0.77 ± 0.0042 day. The TESS observations indicate a rotational period of around $0.770\,44 \pm 0.00009$ day, and this result is statistically consistent with previous results. We summarized the rotational periods obtained from the different data sets in Table 2.

Table 2
Rotational Period in Different Survey

Survey	Filter	$f_{\rm rot}$ ($\rm day^{-1}$)	Period (day)	Period Error (day)	Remark
ASAS-SN	*V*	1.298 532 7	0.7701	0.0002	bc,APOGEE
	V	1.298 364 1	0.7702	0.0001	bd,APOGEE
	V	1.298 414 6	0.770 17	0.000 13	bd,ASAS-SN DR9
NOWT	*U*	1.301 752 6	0.768 205 3	0.002 797 0	
	B	1.299 148 6	0.769 740 0	0.001 990 4	
	V	1.300 850 6	0.768 734 9	0.002 346 2	
	R	1.298 826 7	0.769 933 4	0.002 434 6	
	I	1.300 824 0	0.768 753 1	0.002 715 8	
SuperWASP		1.298 701 3	0.77	0.0042	
TESS		1.297 959 6	0.770 44	0.000 09	

Note. This table summarizes the results of the rotational periods of HD345439 from the different data sets. The first column listed the names of the surveys; the filters that were adopted by the surveys are listed in the second column, and the rotational frequencies are listed in the third column. The rotation periods and corresponding errors are listed in columns 4 and 5. The sources of the data are listed in the last column.

Table 3
Frequencies of Multicolor NOWT Photometry

Filter	Frequency ($\rm day^{-1}$)	SNR	Period (day)	Period Error (day)	Identification	Amplitude (mmag)
U	1.301 752 6	4.519 14	0.768 205 3	0.002 797 0	F0	21.4193
	3.553 567 9	4.815 88	0.281 407 6	0.000 269 8	F1	16.4068
B	1.299 148 6	3.721 38	0.769 740 0	0.001 990 4	F0	12.5016
V	1.300 850 6	4.698 33	0.768 734 9	0.002 346 2	F0	18.6534
R	1.298 826 7	11.985 61	0.769 933 4	0.002 434 6	F0	49.2253
	3.904 816 6	4.206 55	0.256 094 1	0.000 207 5	3F0	13.3104
	6.519 143 0	4.059 02	0.153 394 4	0.000 054 6	5F0	9.4123
	2.607 657 2	8.568 65	0.383 486 1	0.000 193 0	2F0	11.2453
	6.412 435 8	5.424 34	0.155 947 0	0.000 023 6	5F0	5.2630
I	1.300 824 0	6.913 53	0.768 753 1	0.002 715 8	F0	31.7706
	3.967 513 1	4.340 97	0.252 047 2	0.000 217 4	3F0	14.8548
	9.110 771 0	4.140 31	0.109 760 2	0.000 010 0	7F0	3.4015

Note. The results of searching the rotational period of HD345439 in multi-color photometry.

We extract the rotational frequencies from the NOWT photometric data in each band, which are denoted as F0 in Table 3. The corresponding rotational periods of each band are listed in the fourth column of the table. The photometry data of each band exhibits a clear signature at around 0.7691 ± 0.0025 day; however, the signal-to-noise ratio (SNR) in the *B* band is low. The consistency of all observations indicates that the rotational period of HD 345439 is 0.7699 ± 0.0014 day, which is consistent with the value of 0.7701 ± 0.0001 derived by Wisniewski et al. (2015) and the value of $0.770\,18 \pm 0.00002$ day derived by Hubrig et al. (2017a).

3.2. Pulsating Behavior

We utilized the PERIOD04 software (Lenz & Breger 2005) to analyze the TESS and NOWT photometric data for investigating the pulsating behavior of HD 345439. The Nyquist frequency of the TESS observations is $f_{\rm N} = 360\ \rm day^{-1}$; thus, the frequencies in the range of $0 < f < 360\ \rm day^{-1}$ were removed from our analysis. We calculate the resolution frequency $f_{\rm res} = 1/T$ (T represents the duration of the observations) and use this information to distinguish between two contiguous frequencies. If the difference between two contiguous frequencies is less than $f_{\rm res}$, we consider them to be unresolved. The rectified light curve is fitted using the following formula:

$$m = m_0 + \sum_{i=1}^{N} A_i \sin\left(2\pi\left(f_i t + \phi_i\right)\right) \quad (1)$$

where m_0 is the zero-point, A_i is the amplitude, f_i is the frequency, and ϕ_i is the corresponding phase. The multi-frequency least-square fit of the light curve for all detected

significant frequencies is then performed using Equation (1) to obtain the solution for all frequencies. The following search is conducted with the residual data that is obtained by subtracting the above solution from the rectification data. We adopt SNR $\geqslant$4, which is the criterion suggested by Breger et al. (1993), to detect the significant frequencies.

We identify the significant frequencies in the multicolor NOWT photometry data; the Fourier amplitude spectrum of each band is shown in Figure 4. All significant frequencies are obtained according to the $f_{\rm res} = 0.09\ {\rm day}^{-1}$ and SNR $\geqslant 4$ restrictions, which are listed in Table 3. We find an independent frequency in the U band. However, this independent frequency is not detected in the other bands, which indicates that it may be an instrumental artifact. Regarding the B, V, R, and I bands, only the harmonics of the fundamental rotational frequency are detected.

The Fourier amplitude spectra of the TESS photometric data are shown in Figure 5. In addition to the rotational frequency, 39 significant frequencies are detected from the TESS photometric observations. Among these, 15 significant frequencies were removed after taking into account the $f_{\rm res} = 0.04\ {\rm day}^{-1}$ restriction. The remaining frequencies are listed in Table 4; the corresponding SNR values, amplitudes, identifications, and periods are provided in columns 3–6, respectively. All the resolved significant frequencies are identified as the harmonics of the rotational frequency, and no evidence of pulsating behavior is found in HD 345439.

3.3. Morphology of the Light Curve

The light curves of all new archival observations are shown in Figure 3. We calculate the median magnitude in bins of 0.02-phase width and overlay these median values on the initial phase diagram to aid in the visual interpretation of the SuperWASP observations. The light curves show an analogical variation with a feature of the S-wave, and the maximum amplitude $\sim$0.1 mag. The multicolor NOWT photometry is shown in Figure 6. The profiles and amplitudes of the light curves are approximately consistent with the archival observations.

The shapes of the light curves of all photometric observations show a typical double S-wave feature. The light curve obtained from the TESS observations exhibits a pronounced asymmetry between the primary and secondary eclipses. The same asymmetric components are detected in the multicolor observations. An unequal spacing between the primary and secondary eclipses is visible in each band, and the secondary eclipse is delayed with respect to the primary one by a phase of $\sim$0.4. The presence of these unequal spacings constitutes a strict constraint for the shape and density profile of the magnetosphere clouds as well as a restriction on the magnetic obliquity angle β and the rotational inclination angle i. On the other hand, the multicolor NOWT photometry light curves show a different trend in the phase 0.1 to 0.2, compared with that of other photometric

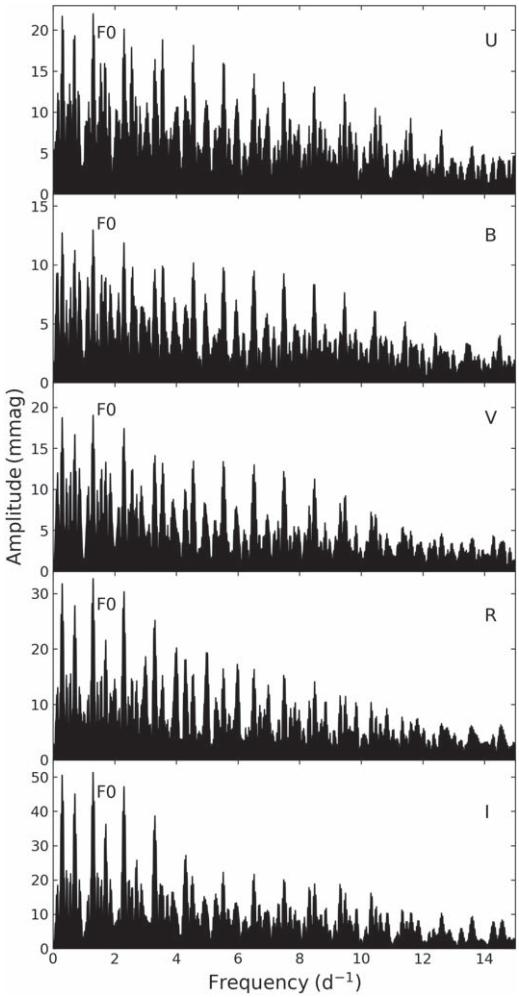

Figure 4. Fourier amplitude spectra for multicolor NOWT light curve of HD 345439. The top panel shows the Fourier amplitude spectrum of the U band. The middle panels show the Fourier amplitude spectra of B, V, and R bands. The bottom panel shows the Fourier amplitude spectrum of the I band. The rotational frequency is marked in each spectrum.

observations, and the amplitude variation decreases with the increase in the central wavelength of the filter. This feature region is marked between two vertical red dashed lines in Figure 6. The same trend does not appear in the other archival observations. Regarding the ASAS-SN and SuperWASP observations, it is the low time resolution that causes the absence of this amplitude variation. The bandpass of the TESS detector ranges from 600 to 1000 nm, and the central wavelength is 786.5 nm (Ricker et al. 2015). However, the variability of the multicolor NOWT photometry at the 0.15 phase is considerably reduced in the I band; therefore, the amplitude variation is unobservable for the TESS detector. The amplitude variation of the multicolor light curves suggests that the material in the magnetic clouds may condense into larger particles, thereby causing an increase in the short-wavelength opacity.

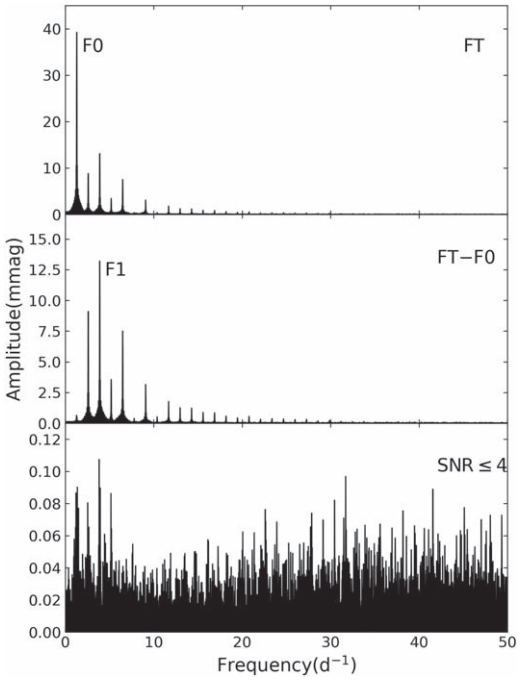

Figure 5. Fourier amplitude spectra and the prewhiten process for the TESS light curve of HD 345439. The top panel shows the rotational frequency F0, the middle panel shows the other harmonics of the rotational frequency, and the bottom panel shows the residual after subtracting all significant frequencies.

3.4. Centrifugal Breakout

Being the archetype of helium-rich stars with large-scale magnetic fields, σ Ori E was conformed to have hard X-ray flares (e.g., Groote & Schmitt 2004; Sanz-Forcada et al. 2004). Townsend & Owocki (2005, hereafter referred to as TO05) speculated that the X-ray flares are associated with the centrifugal breakout and are universal in rapidly rotating magnetic early B star. Subsequently, ud-Doula et al. (2006, hereafter referred to as UD06) demonstrated the feasibility of centrifugal breakout hypothesis via numerical magnetohydrodynamic (MHD) simulations.

In this study, we explore the existence of centrifugal breakout of HD 345439 using the TESS photometric data. We use the functions in the LK package to prewhiten the TESS light curve for eliminating the instrumental variations, and the result is shown in the upper panel of Figure 7. After subtracting the light curve with the periodic signal, the residual magnitudes are shown in the bottom panel of Figure 7. As estimated by TO05 and UD06 works, the entire centrifugal breakout event would occur on a timescale of days. However, apart from the variation caused by the magnetosphere, the smoothed light curve shown in the bottom panel of Figure 7 is relatively devoid of features. Indeed, the residual magnitudes do not vary significantly. Additionally, no systematic variations are observed at the extremum of the light curve. It can thus be inferred that no centrifugal breakout episodes occurred during the TESS photometric observations.

3.5. Stellar Parameters

The luminosity is derived by using the bolometric correction (BC), and the extinction coefficient A_V is estimated from the intrinsic color $(B-V)_0$. The distance modulus (DM) is evaluated using the distance from Gaia DR2. The Gaia DR2 distances are corrected using a weak distance prior that varies smoothly as a function of Galactic longitude and latitude according to a galaxy model (Bailer-Jones et al. 2018). The intrinsic color $(B-V)_0$ is determined from the smooth interpolation of the grids provided by Lanz & Hubeny (2007). We use the relationship of $R(V) \equiv A(V)/E_{(B-V)} = 3.1$ (Cardelli et al. 1989) to derive the extinction coefficient A_V. The solar values, including $BC_{V,\odot} = -0.19$ mag, $M_{\mathrm{bol},\odot} = 4.60$ mag, $M_{V,\odot} = 4.83$ mag, and $V_\odot = -26.74$ mag were taken from a previous work (Torres 2010). The absolute visual magnitude $(M_V = V - A_V - \mathrm{DM})$, the bolometric magnitude $(M_{\mathrm{bol}} = M_V + \mathrm{BC})$, and the luminosity $[\log(L/L_\odot) = 0.4\times(M_{\mathrm{bol},\odot} - M_{\mathrm{bol}})]$ are compiled in Table 5.

We download the grids of ATLAS9 model atmospheres (Castelli & Kurucz 2003) from the ATLAS websites.[7] The grids include the effective temperature (T_{eff}) spanning a range of 15,000–35,000 K with a step of 1000 K, the log g in the range of 2.50–5.00 dex with a step of 0.50 dex, and the metal abundance in the range of −4.00–5.00 dex. The SPECTRUM program (Gray & Corbally 1994) was adopted to synthesize the spectral templates. The unbroadened infinite-resolution spectra were transformed into low resolution ($R \sim 1800$) spectra to be comparable with the LAMOST-LRS. To ensure the accuracy of analysis, we removed the spectral region with wavelength below 390 nm, which is affected by instrumental ripples, and truncated the spectrum at 700 nm. For determining the stellar atmospheric parameters, we matched the LAMOST-LRS spectrum with templates using a methodology similar to LSP3. The LSP3 adopts a cross-correlation algorithm to determine stellar radial velocity and uses the weighted means of parameters of the best-matching templates and values yielded by χ^2 minimization (Xiang et al. 2015). The χ^2 values calculated from the observing spectrum and matching template spectra are defined as:

$$\chi^2 = \sum_{i=1}^{N} \frac{(O_i - T_i)^2}{\sigma_i^2} \quad (2)$$

where O_i is flux densities of the observing spectrum of the ith, T_i is flux densities of the template spectra of the ith. N is the total pixel number used to calculate the χ^2 values, and σ_i is the error of flux density of the observing spectrum of the ith pixel.

[7] https://wwwuser.oats.inaf.it/castelli/grids.html

Table 4
All Frequencies Detected in Photometric Data of TESS

No.	Frequency (day^{-1})	SNR	Amplitude (mmag)	Identification	Period (day)
1	1.297 952 32	262.9869	39.214 640 9	F0	0.770 444 336
2	3.891 975 88	84.069 76	13.203 390 9	3F0	0.256 938 9
3	2.595 904 65	170.524 81	9.086 189 12	2F0	0.385 222 162
4	6.487 880 53	160.280 67	7.542 532 58	5F0	0.325 243 263
5	5.189 928 21	113.873 92	3.356 800 69	4F0	0.192 680 893
6	9.083 785 18	151.640 49	3.221 736 86	7F0	0.110 086 267
7	11.679 689 8	69.026 96	1.808 459 48	9F0	0.085 618 712
8	12.977 642 2	51.920 77	1.282 990 03	10F0	0.077 055 6
9	14.275 594 5	54.0551	1.244 646 12	11F0	0.070 049 622
10	15.573 546 8	40.945 05	0.879 632 814	12F0	0.064 211 449
11	16.871 499 1	38.710 91	0.843 725 336	13F0	0.059 271 556
12	18.171 332 5	28.109 08	0.582 071 681	14F0	0.055 031 737
13	20.769 118 3	24.244 62	0.548 933 463	16F0	0.048 148 409
14	10.381 737 5	26.154 45	0.479 181 066	8F0	0.096 322 99
15	19.467 403 8	21.346 88	0.427 989 186	15F0	0.051 367 918
16	3.918 311 15	14.4029	0.462 188 854	3F0	0.255 211 994
17	23.363 141 8	14.633 46	0.377 758 953	18F0	0.042 802 462
18	24.664 856 4	13.823 55	0.336 342 688	19F0	0.040 543 516
19	7.787 713 95	16.505 72	0.332 816 778	6F0	0.128 407 387
20	27.262 642 1	11.7586	0.297 142 974	21F0	0.036 680 231
21	22.063 308 4	11.217 28	0.296 931 562	17F0	0.045 324 118
22	25.960 927 6	13.240 85	0.281 336 096	20F0	0.038 519 425
23	29.858 546 7	9.319 29	0.231 048 733	23F0	0.033 491 248
24	28.556 832 2	7.196 75	0.180 087 489	22F0	0.035 017 89
25	33.748 641 5	6.3148	0.158 025 325	26F0	0.029 630 822

Note. All frequencies that are detected in the photometric data of TESS are listed in the table. We calculated the corresponding period for each frequency, and identified their nature as independent frequencies, harmonics, or combinations.

As shown in Figure 8, the best fitting result reproduces with the effective temperature at 22 ± 1 kK, log $g = 4.00 \pm 0.22$ and $[\mathrm{Fe/H}] = -0.50$ dex.

A grid of evolution tracks with a mass ranging from $4\,M_{\odot}$ to $10\,M_{\odot}$ with a step of $0.02\,M_{\odot}$ was generated using the Modules for Experiments in Stellar Astrophysics (MESA) (Paxton et al. 2011, 2013, 2015, 2018, 2019). The rotational effect of the star having $v/v_{\mathrm{crit}} = 0.75$, a restriction which is imposed by photometric observations, was used in the grid. The luminosity, mass, and age of HD 345439 were estimated from its location on the Hertzsprung−Russell diagram (HRD) with the evolutionary tracks. The positions of HD 345439 on the Kiel diagram (KD) and HRD are shown in Figure 9. The mass, luminosity, and age were derived as $M = 8.00\,^{+0.50}_{-0.51}\,M_{\odot}$, log $(L/L_{\odot}) = 3.82 \pm 0.1$ dex, and $\tau_{\mathrm{age}} = 26.79\,^{+7.03}_{-6.79}$ Myr, respectively. According to the StefanBoltzmann law, the radius was estimated to be $5.59 \pm 0.06\,R_{\odot}$.

4. Discussion

4.1. Parameters Restriction Under the RRM Model

Following a previous report (Nakajima 1985), the TO05 work developed an RRM model to interpret the interaction of the magnetosphere with other phenomena in hot stars and indicated that magnetospheric clouds are the primary factor responsible for the variation in the light curve of rapidly rotating magnetic stars.

By applying the light-curve synthesis demonstrated by the UD06 work[8], we obtained the shapes of light curves based on the RRM model. Since the light-curve synthesis does not provide the absolute flux, we used the normalized flux converted to the corresponding Δmag. To generate the theoretical light curves, we used a grid with the rotational factor (v/v_{crit}) in the range from 0.00 to 0.99 with a step of 0.25, the magnetic obliquity angle β in the range of $0^{\circ} \sim 90^{\circ}$ with a step of 15°, and the rotational inclination angle i in the range of 0°–90° with a step of 15°. For the accuracy of the analysis, we used the light curves obtained from the TESS observations and the multicolor NOWT photometry. The χ^2-minimum method was used to estimate the difference between the RRM model and the observations. Figure 10 shows the comparison between the photometry light curves and the light curves synthesized using the RRM model. The best fit (black line) indicates that we can restrict the magnetic obliquity angle β and the rotational inclination angle i to the values satisfying the approximate relation $\beta + i \approx 105^{\circ}$($i = 75^{\circ}$ and $\beta = 30^{\circ}$)

[8] http://www.astro.wisc.edu/~townsend/static.php?ref=rrm-movies

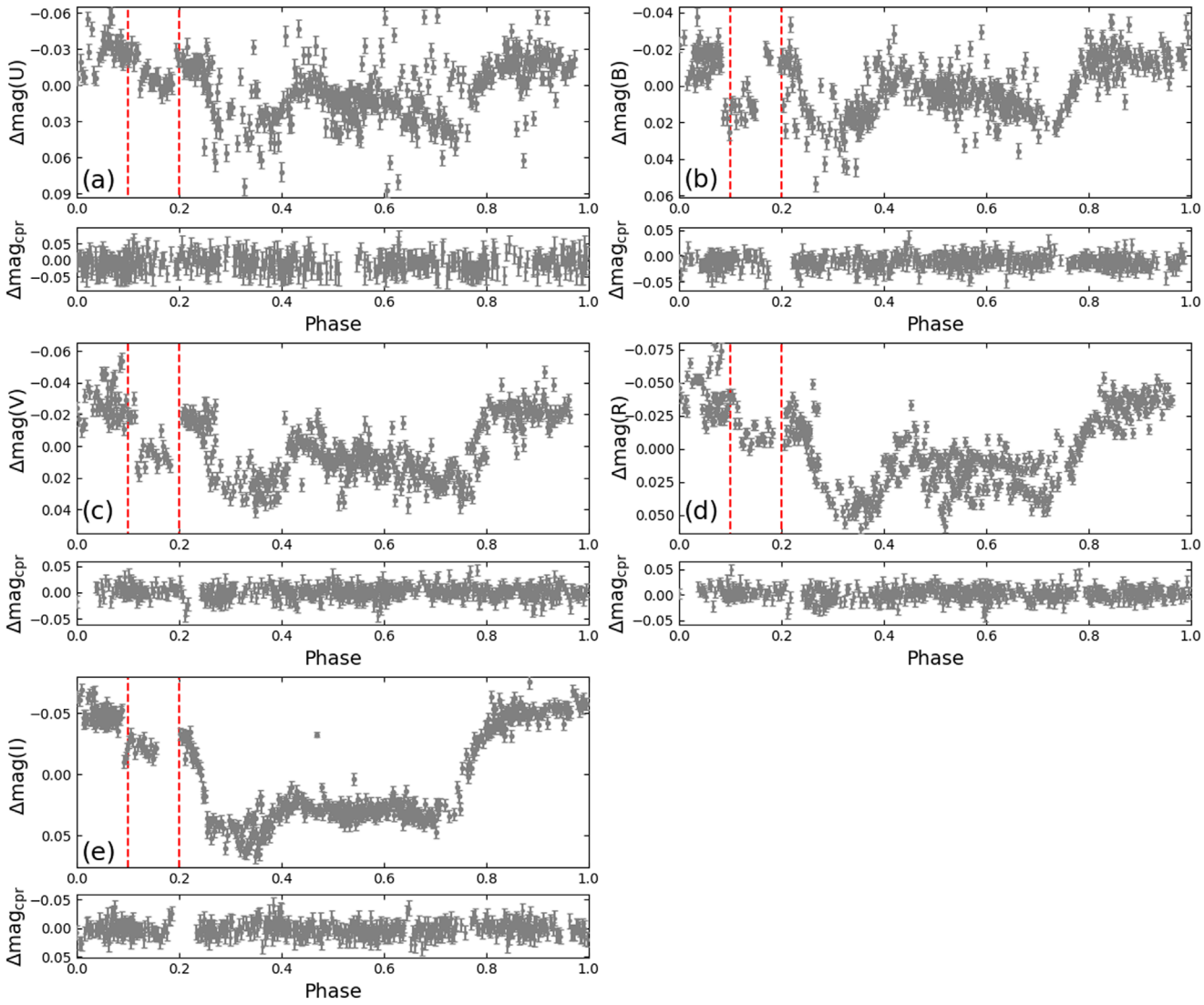

Figure 6. Phase diagram of multicolor photometric observations with NOWT. A phase fold has been preformed for each band with the corresponding period. The light curves of the comparison star are shown under the light curves of HD 345439. The vertical red dashed lines marked the parts of the light curves where the differences compared to the light curves were predicted by the RRM model.

Based on the work by Shultz et al. (2020), we also adopt the assumptions that $i = 60°$ and $\beta = 45°$. However, there are several differences between the simulated result and photometric observations. The unequal eclipses may be caused by the mismatch parameters with the magnetic obliquity angle β and the rotational inclination angle i (Townsend et al. 2005). Our result is more consistent with that reported by Hubrig et al. (2017a).

Although we are able to reproduce the light curve for HD 345439, there are evident discrepancies between the theoretical and observational light curves. In contrast to the synthesized light curves, asymmetrical depths of eclipses are detected in the observational light curves. Townsend et al. (2005) pointed out that this asymmetry in the eclipses may be caused by an offset between the center of the dipole magnetic fields and the rotation axis. Furthermore, in the phase range of 0.3–0.7, the observational and synthesized light curves show opposite trends. One hypothesis that could explain this discrepancy is that the magnetosphere clouds of HD 345439 have more complex geometries, as was also reported by Carciofi et al. (2013). In the 0.3–0.7 phase, the magnetospheric column density is affected by other small scale magnetic fields, which results in larger density values than those estimated by the RRM model. The TO05 work presented the morphology of magnetic clouds with pure poloidal magnetic fields. Nevertheless, the MHD simulations show that in order to maintain stable global scale magnetic

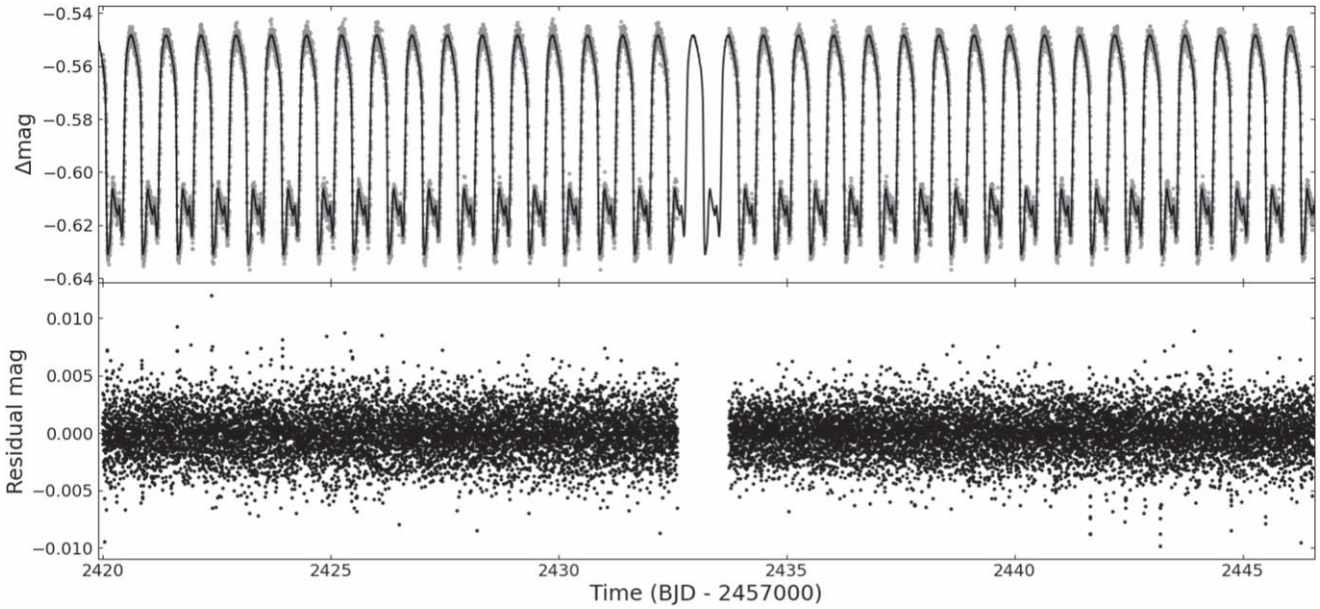

Figure 7. Upper panel: prewhitened light curve of HD 345439. Bottom panel: residual magnitudes after subtracting the light curve with the periodic signal.

Table 5
Stellar Parameters of HD 345439

Sp. type[1]	B2V		
π(mas)[2]	0.3739 ± 0.0192		
Dis. (pc)[3]	$2141.85^{+214.64}_{-179.54}$		
Photometric	Our Work	Shultz[4]	
$(B-V)_0$ (mag)	-0.245	⋯	
$E_{(B-V)}$ (mag)	0.745 ± 0.016	⋯	
A_V(mag)	2.31 ± 0.05	2.2 ± 0.1	
BC(mag)	-2.11 ± 0.11	-2.4 ± 0.4	
M_V(mag)	-2.85 ± 0.16	-2.9 ± 0.3	
$M_{\rm bol}$(mag)	-4.96 ± 0.25	-5.3 ± 0.7	
$P_{\rm rot}$ (day)	0.7699 ± 0.0014		
Physical			Guo[5]
$T_{\rm eff}$ (kK)	22 ± 1^L	23 ± 2^N	22 ± 1.5^N
log$g$(cgs)	4.00 ± 0.22^L	4.29 ± 0.19^N	3.67 ± 0.25^N
$\log(L/L_\odot)$	3.82 ± 0.1	4.0 ± 0.3	$4.01^{+0.33}_{-0.17}$
[Fe/H](dex)	-0.5	⋯	-0.35
$M/M_\odot$	$8.00^{+0.50}_{-0.51}$	$8.99^{+1.02}_{-1.19}$	$8.59^{+2.00}_{-1.00}$
$R/R_\odot$	5.59 ± 0.06	$6.29^{+0.93}_{-1.83}$	$7.00^{+3.21}_{-1.30}$
$\tau_{\rm age}$ (Myr)	$26.79^{+7.03}_{-6.79}$	$22.50^{+0.09}_{-5.23}$	$26.52^{+6.60}_{-7.78}$

Note. References: [1] Eikenberry et al. (2014), [2] Gaia Collaboration (2020), [3] Bailer-Jones et al. (2018), [4] Shultz et al. (2019b), [5] Guo et al. (2021). [N] represents the parameter determined from NLTE models, [L] represents the parameter determined from LTE models.

fields on long timescale, the ratio of the energies of toroidal and poloidal components of the magnetic fields must have a specific value (Braithwaite 2009; Duez et al. 2010). On the other hand, the opposite trend may be caused by chemical anomalies and starspots, which are from microscopic chemical transport processes. It is thus necessary to determine the surface chemical spot structure using Doppler imaging (DI) to further restrict the light curve of HD 345439 (e.g., Kochukhov et al. 2022).

4.2. Mass Leakage Process

No evidence of centrifugal breakout was found in the TESS photometry. Several factors could explain the failure of the RRM model in detecting the centrifugal breakout. One of the reasons is that no relevant scheduling of the TESS run was suitable for searching for the centrifugal breakout. Another factor could be that the mass of the magnetic clouds does not reach the crucial value necessary to generate the centrifugal breakout. The TO05 work predicted that the crucial mass was dependent strongly on the magnetic strength, stellar radius, mass-loss rate, and escape velocity. HD 345439 has a more extreme state than σ Ori E; thus, its breakout timescale is larger than the latter with a low incidence of breakout episode.

Although the centrifugal breakout is a natural result in MHD for rapidly rotating magnetic stars (ud-Doula et al. 2006), no centrifugal breakout event was detected for HD 345439. A uniform situation occurred in σ Ori E, which indicates the low incidence of events (Townsend et al. 2013). In addition to the centrifugal breakout, the ongoing reductions in the magnetospheric column density might indicate the mass leakage of the magnetosphere. Owocki & Cranmer (2018) presented diffusion-plus-drift magnetospheres (DDM) model to interpret the mass leakage of magnetic hot stars. In this scenario, plasma

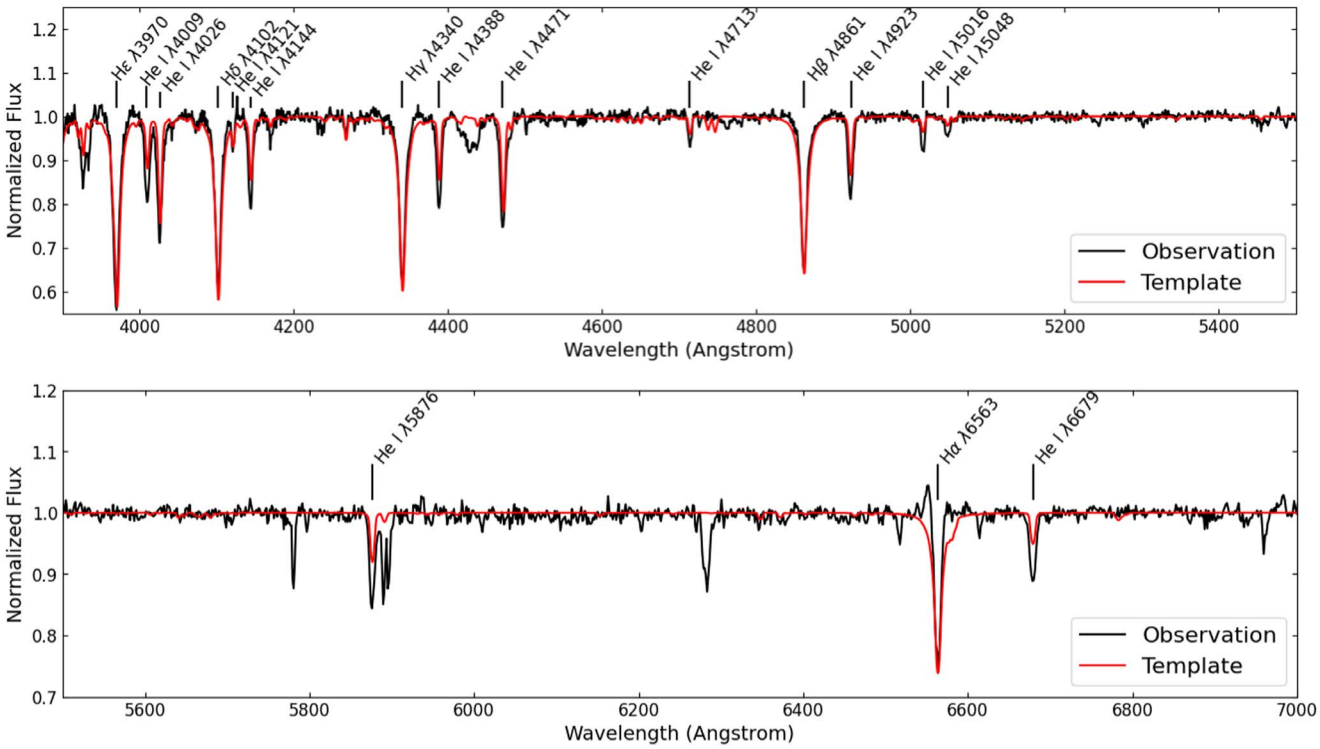

Figure 8. LAMOST-LRS spectrum of HD 345439. The identified lines were marked in the panels. The black line represents the observed spectrum, and the red line represents the template spectrum. We truncate the wavelength at 700 nm, and show the results in two panels.

diffuses in both directions and escapes from the star via drift. The mass leakage process in the DDM model is more gradual than in the RRM model, and in particular the centrifugal breakout does not occur in the DDM model. Shultz et al. (2020) analyzed the Hα line profiles of the magnetic B-type stars, and pointed out that the Hα emission and strength are independent of the effective temperature, luminosity, and mass-loss rate; these results support the hypothesis of the occurrence of centrifugal breakout events. However, Shultz et al. (2020) also reported that centrifugal breakouts must be a continuous process, and the Hα emission is in contradiction with the model predictions. The detection of the centrifugal breakout using the TESS data presented in this work supports the results of Shultz et al. (2020).

4.3. Discrepancies in the Stellar Parameters

We obtained the stellar parameters of HD 345439 from the LAMOST-LRS spectrum. The basic parameters were also measured by previous works: Guo et al. (2021) derived $T_{\rm eff} = 22 \pm 1.5$ kK, log $g = 3.67 \pm 0.25$, and [Fe/H] $= -0.35$ dex with the Stellar LAbel Machine (SLAM). The SLAM (Zhang et al. 2020) is a data-driven method based on support vector regression (SVR) which is a robust nonlinear regression technique and often used to build the mapping from stellar spectra to stellar labels in previous works (e.g., Bu & Pan 2015; Lu & Li 2015). Shultz et al. (2020) determined $T_{\rm eff} = 23 \pm 2$ kK, log $g = 4.29 \pm 0.19$, and log $(L/L_{\odot}) = 4.0 \pm 0.3$ dex from the Gaia photometric observations and high-resolution NLTE atmosphere spectra. Regarding the LAMOST-LRS spectrum, it should be noted that the lowest value of the surface gravity was obtained from the NLTE atmosphere using the SLAM, while the highest value was from the LTE atmosphere. A similar discrepancy occurred for other hot stars (e.g., Shultz et al. 2021). As one of the main reasons, we adopted a different atmospheric model, which indicated the different line list, model atoms, and opacity will be used to generate final template spectra. Second, there are differences in the method of how to derive the stellar parameters of HD 345439. Different grids were used between our study and Guo et al. (2021) to increase the difference in the surface gravity. The surface gravity and effective temperature derived in the present work are consistent with the results of Shultz et al. (2020).

The locations of HD 345439 derived from the NLTE and LTE atmospheres are marked in Figure 9. The mass, radius, and age were also derived using the evolution tracks in the HRD, and the final results are listed in Table 5. Being a magnetic He-rich star, HD 345439 is located in the colony of other main-sequence (MS) magnetic He-rich stars on the HRD

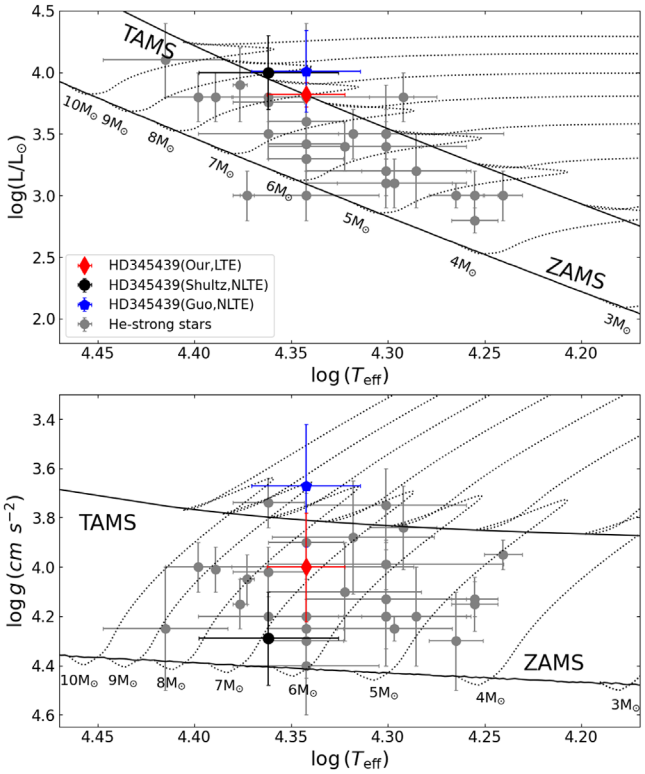

Figure 9. Hertzsprung-Russell diagram (top panel) and Kiel diagram (bottom panel). The position of HD 345439 is marked with the results of both the LTE and NLTE. The red diamond indicates the result derived from the LTE model. The black dot and blue pentagon represent the results derived from the NLTE models. The locations of the He-rich stars are marked with gray dots. For HD 345439, the red diamond represents the result of this work, the blue pentagon represents the result of Guo et al. (2021), and the black dot represents the result of Shultz et al. (2019b). The parameters of other He-rich stars were obtained from Shultz et al. (2019b).

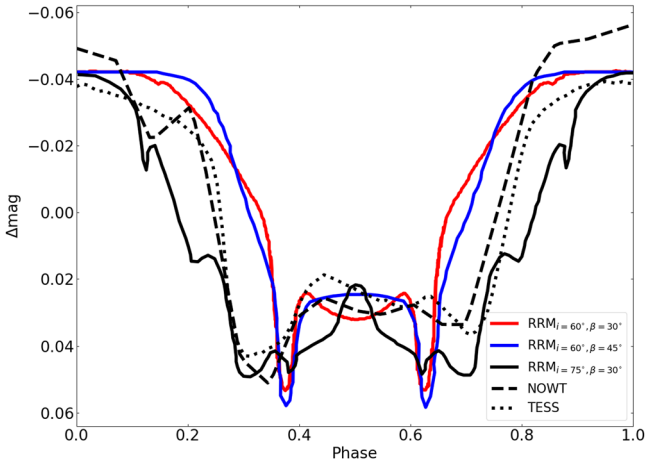

Figure 10. Light curves derived from the photometric observations and synthesized with the RRM model. The bule line represents the light curve that was synthesized with the RRM model using the parameters taken from Shultz et al. (2020). The black line represents the light curve that was synthesized with the RRM model using the parameters taken from Hubrig et al. (2017a). We adjusted the parameters to reproduce the variations at the 0.5 phase (red line). The dotted and dashed lines represent the TESS and NOWT photometric observations, respectively.

and KD. HD 345439 is around the terminal-age main sequence (TAMS), which suggests that HD 345439 is an old B-type star. HD 345439 has a larger surface gravity than that inferred from its luminosity derived from the NLTE or LTE atmosphere. The other magnetic He-strong early-type stars are also marked in the HRD and KD. The locations of the He-strong stars in the HRD and KD are also characterized by systematic discrepancies. We also mark the other magnetic He-strong early-type stars on the HRD and KD. The locations of He-strong stars between the HRD and KD also have systematic discrepancies.

The surface gravity of magnetic early-type stars is usually inferred from the pressure broadening of some specific H and He lines (e.g., Cidale et al. 2007; Sikora et al. 2015). Strong magnetic fields contribute to the magnetic pressure via the Lorentz force, which results in the flux of the spectral lines changing by several percent. Additionally, the magnetic clouds reduce this flux by approximately 2% (Valyavin et al. 2004; Vallverdú et al. 2014; Shultz et al. 2019a, 2020). The flux variations result in a larger value of the surface gravity inferred from the template, and it can be seen that 0.2 dex variations in the surface gravity result in a mass uncertainty as high as ∼20%. On the other hand, $\tau_{\rm age}$ of HD 345439 has ∼30% uncertainty caused by the uncertainty in both log $(L/L_{\odot})$ and $T_{\rm eff}$. Although the number of magnetic stars are growing, only a dozen rapidly rotating magnetic stars have been confirmed at the moment. It is important to obtain a detailed characterization of all known samples for understanding the evolution of rapidly rotating magnetic stars. Thus, more future works are required to perform further photometric observations of rapidly rotating magnetic stars and search for more samples for this type of star (e.g., Bagnulo et al. 2006; Hubrig et al. 2013).

5. Summary

Based on the photometric data obtained from the NOWT observations and new archives, we calculated the rotational period of HD 345439 to be 0.7699 ± 0.0014 days. Our results are consistent with those of Wisniewski et al. (2015) and Hubrig et al. (2017a). In addition, no pulsating behavior was detected in HD 345439. We compared the light curves obtained from the photometric observations with those synthesized under the assumptions of the RRM model. The asymmetric components in the light curves of HD 345439 may be caused by an offset between the center of the dipolar magnetic fields and the rotation axis. The unequal spacing of the eclipses was restricted by the relation $\beta + i \approx 105°$. No centrifugal breakout events were detected in the photometric observations possibly because of the lack of an adequate scheduling of the TESS or

the fact that the magnetic clouds could not reach the critical mass. We derived the stellar parameters from the LAMOST-LRS spectrum and compared them with the results obtained from the NLTE atmosphere. The obtained stellar parameters are consistent with those reported by Shultz et al. (2019b) while they are in slight disagreement with those of Guo et al. (2021). These discrepancies are caused by the differences between the NLTE and LTE atmospheres as well as the method adopted to derive the physical parameters. On the other hand, the SLAM can only derive the local optimal solution for the LAMOST-LRS spectrum of HD 345439.

Acknowledgments

This work received the generous support of the Natural Science Foundation of Xinjiang No. 2021D01C075, the National Natural Science Foundation of China under grants U2031204, 12163005 and 11863005. We gratefully acknowledge the science research grants from the China Manned Space Project with Nos. CMS-CSST-2021-A08 and CMS-CSST-2021-A10. J. Z.L. acknowledges the science research grants from National Key R&D Program of China (2022YFE0126200). Guo Shou Jing Telescope (the Large Sky Area Multi-Object Fiber Spectroscopic Telescope LAMOST) is a National Major Scientific Project built by the Chinese Academy of Sciences. Funding for the project has been provided by the National Development and Reform Commission. LAMOST is operated and managed by the National Astronomical Observatories, Chinese Academy of Sciences. This paper includes data collected with the TESS mission, obtained from the MAST data archive at the Space Telescope Science Institute (STScI). Funding for the TESS mission is provided by the NASA Explorer Program. STScI is operated by the Association of Universities for Research in Astronomy, Inc., under NASA contract NAS 526555.

References

Astropy Collaboration, Price-Whelan, A. M., Sipőcz, B. M., et al. 2018, AJ, 156, 123
Astropy Collaboration, Robitaille, T. P., Tollerud, E. J., et al. 2013, A&A, 558, A33
Babcock, H. W. 1947, ApJ, 105, 105
Bagnulo, S., Landstreet, J. D., Lo Curto, G., Szeifert, T., & Wade, G. A. 2003, A&A, 403, 645
Bagnulo, S., Landstreet, J. D., Mason, E., et al. 2006, A&A, 450, 777
Bai, C.-H., Feng, G.-J., Zhang, X., et al. 2020, RAA, 20, 211
Bailer-Jones, C. A. L., Rybizki, J., Fouesneau, M., Mantelet, G., & Andrae, R. 2018, AJ, 156, 58
Bailey, J. D., Landstreet, J. D., Bagnulo, S., et al. 2011, A&A, 535, A25
Bohlender, D. A., & Monin, D. 2011, AJ, 141, 169
Borra, E. F., & Landstreet, J. D. 1980, ApJS, 42, 421
Braithwaite, J. 2009, MNRAS, 397, 763
Breger, M., Stich, J., Garrido, R., et al. 1993, A&A, 271, 482
Bu, Y., & Pan, J. 2014, MNRAS, 447, 256
Butters, O. W., West, R. G., Anderson, D. R., et al. 2010, A&A, 520, L10
Carciofi, A. C., Faes, D. M., Townsend, R. H. D., & Bjorkman, J. E. 2013, ApJL, 766, L9
Cardelli, J. A., Clayton, G. C., & Mathis, J. S. 1989, ApJ, 345, 245
Castelli, F., & Kurucz, R. L. 2003, in Modelling of Stellar Atmospheres, Vol. 210, ed. N. Piskunov, W. W. Weiss, & D. F. Gray, A20
Cidale, L. S., Arias, M. L., Torres, A. F., et al. 2007, A&A, 468, 263
Cui, X.-Q., Zhao, Y.-H., Chu, Y.-Q., et al. 2012, RAA, 12, 1197
Duez, V., Braithwaite, J., & Mathis, S. 2010, ApJL, 724, L34
Eikenberry, S. S., Chojnowski, S. D., Wisniewski, J., et al. 2014, ApJL, 784, L30
Folsom, C. P., Kochukhov, O., Wade, G. A., Silvester, J., & Bagnulo, S. 2010, MNRAS, 407, 2383
Fossati, L., Castro, N., Morel, T., et al. 2015, A&A, 574, A20
Fossati, L., Zwintz, K., Castro, N., et al. 2014, A&A, 562, A143
Gaia Collaboration 2020, yCat, I/350 652, A2
González, J. F., Briquet, M., Przybilla, N., et al. 2019, A&A, 626, A94
González, J. F., Hubrig, S., Przybilla, N., et al. 2017, MNRAS, 467, 437
Gray, R. O., & Corbally, C. J. 1994, AJ, 107, 742
Groote, D., & Schmitt, J. H. M. M. 2004, A&A, 418, 235
Grunhut, J. H., Rivinius, T., Wade, G. A., et al. 2012, MNRAS, 419, 1610
Guo, Y., Zhang, B., Liu, C., et al. 2021, ApJS, 257, 54
Hubrig, S., Kholtygin, A. F., Schöller, M., & Ilyin, I. 2017a, MNRAS, 467, L81
Hubrig, S., Mikulášek, Z., Kholtygin, A. F., et al. 2017b, MNRAS, 472, 400
Hubrig, S., Schöller, M., Ilyin, I., et al. 2013, A&A, 551, A33
Hubrig, S., Fossati, L., Carroll, T. A., et al. 2014, A&A, 564, L10
Jayasinghe, T., Kochanek, C. S., Stanek, K. Z., et al. 2018, MNRAS, 477, 3145
Kochanek, C. S., Shappee, B. J., Stanek, K. Z., et al. 2017, PASP, 129, 104502
Kochukhov, O., Papakonstantinou, N., & Neiner, C. 2022, MNRAS, 510, 5821
Landstreet, J. D., & Borra, E. F. 1978, ApJL, 224, L5
Lanz, T., & Hubeny, I. 2007, ApJS, 169, 83
Lenz, P., & Breger, M. 2005, CoAst, 146, 53
Leone, F., Bohlender, D. A., Bolton, C. T., et al. 2010, MNRAS, 401, 2739
Leto, P., Trigilio, C., Oskinova, L. M., et al. 2018, MNRAS, 476, 562
Lomb, N. R. 1976, Ap&SS, 39, 447
Lu, Y., & Li, X. 2015, MNRAS, 452, 1394
Luo, A. L., Zhao, Y.-H., Zhao, G., et al. 2015, RAA, 15, 1095
Nakajima, R. 1985, Ap&SS, 116, 285
Oksala, M. E., Kochukhov, O., Krtička, J., et al. 2015, MNRAS, 451, 2015
Oskinova, L. M., Hamann, W. R., Cassinelli, J. P., Brown, J. C., & Todt, H. 2011, AN, 332, 988
Owocki, S. P., & Cranmer, S. R. 2018, MNRAS, 474, 3090
Pawlak, M., Pejcha, O., Jakubčík, P., et al. 2019, MNRAS, 487, 5932
Paxton, B., Bildsten, L., Dotter, A., et al. 2011, ApJS, 192, 3
Paxton, B., Cantiello, M., Arras, P., et al. 2013, ApJS, 208, 4
Paxton, B., Marchant, P., Schwab, J., et al. 2015, ApJS, 220, 15
Paxton, B., Schwab, J., Bauer, E. B., et al. 2018, ApJS, 234, 34
Paxton, B., Smolec, R., Schwab, J., et al. 2019, ApJS, 243, 10
Petit, P., Donati, J. F., Oliveira, J. M., et al. 2004, MNRAS, 351, 826
Ricker, G. R., Winn, J. N., Vanderspek, R., et al. 2015, JATIS, 1, 014003
Rivinius, T., Tefl, S. Å., Townsend, R. H. D., & Baade, D. 2008, A&A, 482, 255
Rivinius, T., Townsend, R. H. D., Kochukhov, O., et al. 2013, MNRAS, 429, 177
Sanz-Forcada, J., Franciosini, E., & Pallavicini, R. 2004, A&A, 421, 715
Scargle, J. D. 1982, ApJ, 263, 835
Schnerr, R. S., Henrichs, H. F., Neiner, C., et al. 2008, A&A, 483, 857
Shen, D.-X., Zhang, Y., Li, C.-Y., et al. 2021, RAA, 21, 124
Shultz, M. E., Kochukhov, O., Labadie-Bartz, J., David-Uraz, A., & Owocki, S. P. 2021, MNRAS, 507, 1283
Shultz, M. E., Wade, G. A., Rivinius, T., et al. 2019a, MNRAS, 490, 274
Shultz, M. E., Wade, G. A., Rivinius, T., et al. 2019b, MNRAS, 485, 1508
Shultz, M. E., Owocki, S., Rivinius, T., et al. 2020, MNRAS, 499, 5379
Shultz, M., & Wade, G. A. 2017, MNRAS, 468, 3985
Sikora, J., Wade, G. A., Bohlender, D. A., et al. 2015, MNRAS, 451, 1928
Sikora, J., Wade, G. A., Bohlender, D. A., et al. 2016, MNRAS, 460, 1811
Torres, G. 2010, AJ, 140, 1158
Townsend, R. H. D., & Owocki, S. P. 2005, MNRAS, 357, 251
Townsend, R. H. D., Owocki, S. P., & Groote, D. 2005, ApJL, 630, L81
Townsend, R. H. D., Rivinius, T., Rowe, J. F., et al. 2013, ApJ, 769, 33
ud-Doula, A., Townsend, R. H. D., & Owocki, S. P. 2006, ApJL, 640, L191
Vallverdú, R., Cidale, L., Rohrmann, R., & Ringuelet, A. 2014, Ap&SS, 352, 95

Valyavin, G., Kochukhov, O., & Piskunov, N. 2004, A&A, 420, 993
Wade, G. A., Aurière, M., Bagnulo, S., et al. 2006, A&A, 451, 293
Wade, G. A., Alecian, E., Bohlender, D. A., et al. 2009, The MiMeS project: magnetism in massive stars, in Cosmic Magnetic Fields: From Planets, to Stars and Galaxies, Vol. 259, ed. K. G. Strassmeier, A. G. Kosovichev, & J. E. Beckman, 333
Wade, G. A., Barbá, R. H., Grunhut, J., et al. 2015, MNRAS, 447, 2551
Wade, G. A., Grunhut, J., Gräfener, G., et al. 2012b, MNRAS, 419, 2459
Wade, G. A., Maíz Apellániz, J., Martins, F., et al. 2012a, MNRAS, 425, 1278
Wade, G. A., Shultz, M., Sikora, J., et al. 2017, MNRAS, 465, 2517
Wisniewski, J. P., Chojnowski, S. D., Davenport, J. R. A., et al. 2015, ApJL, 811, L26
Xiang, M. S., Liu, X. W., Yuan, H. B., et al. 2015, MNRAS, 448, 822
Zhang, B., Liu, C., & Deng, L.-C. 2020, ApJS, 246, 9